

Full Length Article

High capacitive performance of hollow activated carbon fibers derived from willow catkins



Kai Wang^{a,b,c,1}, Yan Song^{a,1}, Rui Yan^{a,b}, Ning Zhao^a, Xiaodong Tian^{a,b}, Xiao Li^{a,b}, Quanguo Guo^a, Zhanjun Liu^{a,*}

^a Key Laboratory of Carbon Materials, Institute of Coal Chemistry, Chinese Academy of Sciences, 27 South Taoyuan Road, Taiyuan 030001, PR China

^b University of Chinese Academy of Sciences, Beijing 100049, PR China

^c Institute of Science and Technology, Shanxi Coal Import and Export Group Co., LTD, 115 Changfeng Street, Taiyuan 030006, PR China

ARTICLE INFO

Article history:

Received 11 August 2016

Received in revised form 23 October 2016

Accepted 24 October 2016

Available online 25 October 2016

Keywords:

Supercapacitor

Willow catkins

Potassium hydroxide activation

Hollow activated carbon fibers

ABSTRACT

In this paper, we prepared three different kinds of hollow activated carbon fibers (HACFs) from willow catkins (WCs), phenolic- and pitch-based hollow fibers, respectively. The morphology, pore structure, surface chemical composition and electrochemical properties of these hollow fibers were studied in parallel. Due to its high-hollow, cost-effective as well as eco-friendly nature, HACFs derived from WCs can be served as excellent electrode materials for electrochemical energy storage devices. Electrochemical measurements illustrate that the WCs derived HACFs exhibit not only high specific capacitance of 333 F g^{-1} at 0.1 A g^{-1} but also considerable rate capability with a retention of 62.7% (209 F g^{-1} at 10 A g^{-1}). Symmetric supercapacitor devices that using WCs derived HACFs as electrodes deliver a maximum energy density of $\sim 8.8 \text{ Wh kg}^{-1}$ at power density of 50 W kg^{-1} and good cycling performance with 95.5% retention over 3000 cycles at 5 A g^{-1} in 6 M KOH aqueous electrolytes.

© 2016 Published by Elsevier B.V.

1. Introduction

Climate change and energy consumption of non-renewable fossil fuels have greatly affected the development of economy and circulation of ecological environment. With the increasing need for portable electronic devices and the development of hybrid electric vehicles, environmentally-friendly and powerful energy resources are highly demanded. Electrochemical capacitors (ECs) or supercapacitors have attracted increasing attention in energy storage due to the high power density, rapid charge/discharge capability and long cycle life, etc. [1–3]. Based on the energy storage mechanism, supercapacitors can be divided into two categories: electrochemical double layer capacitance (EDLC) involving physical adsorption of ions from electrolyte and pseudocapacitance involving reversible faradaic redox reactions [4,5]. Currently, most commercial supercapacitors are EDLCs ascribed to their relatively low cost and prominent durability [6–8]. Carbon-based materials including activated carbons and carbon nanomaterials (CNTs, Graphenes) are most widely used as electrodes because of the superior physical and chemical properties, such as low cost, diverse

forms (powders, fibers, tubes, sheets, monoliths, aerogels, composites, etc.) [9–17], ease of processability, controllable porosity, and rich electrochemical active sites. Besides, in terms of both power delivery rate and energy storage capacity, proper control over the specific surface area and pore size suitable to appropriate type of electrolyte solution are vital to ensure a good performance of EDLCs.

In general, commercial activated carbons are the most widely used electrode materials in supercapacitor application. However, most of them are particles and may have different pore structures such as microporous, mesoporous or hierarchical porous that means the coexist of micropores ($< 2 \text{ nm}$), mesopores ($2\text{--}50 \text{ nm}$) and macropores ($> 50 \text{ nm}$), which is ascribed to different preparation processes and different raw materials used. Generally speaking, the mesoporous and hierarchical porous activated carbons offer relatively low specific capacitance ($< 200 \text{ F g}^{-1}$) in aqueous electrolytes due to their relatively broad pore size distribution but low micropores content. It is well known that the energy storage occurs primarily in micropores [18,19]. Carbon materials in the form of fiber may be more effective to produce activated carbon with more micropores which will lead to shortened transport distance for ions from the electrolyte to micropores [20,21]. Hollow micro-/nano-structures are of great interest as a unique family of functional materials with well-defined interior voids and functional shells [22,23]. Their unique structural virtue such as large

* Corresponding author.

E-mail address: zjliu03@sxicc.ac.cn (Z. Liu).

¹ These authors contributed equally to this work.

surface area, high pore volume, and low density endows them with the potential application in many aspects, including catalysis, gas sensors, energy conversion, and storage systems [24–27]. Therefore, there has been an increasing demand for simple and controllable synthesis of hollow nanostructured materials [28,29]. In particular, one-dimensional (1D) hollow tubular structures have been considered as promising hollow structures. e.g. the hollow macro-chamber can ensure ion transportation at high rates and plays the important role of ion reservoir. Lou [22] et al. prepared series of binary-metal sulfides with hollow tubular structures that exhibited excellent electrochemical properties. Therefore, it is also become very attractive to prepare activated carbon fibers with hollow tubular structures, which combines the advantages of activated carbon fibers and peculiar 1D hollow tubular structure.

Besides, when considering the potential scale of supercapacitor applications. Biomass is a cost-effective carbon precursor because it's an environmentally friendly and renewable resource with abundant availability [30–32]. The microstructure and chemical compositions of carbon precursor from biomass have great effect on the morphology, pore structure and surface chemical functional groups of the final porous carbonaceous materials. The cotton-based carbon fibers (CCFs) with hollow tubular structure prepared by carbonizing the cotton fibers in ammonia inherit the natural hollow structure of the cotton fibers. The CCFs have high specific surface area up to $778.6 \text{ m}^2 \text{ g}^{-1}$ and high nitrogen content (3.3 at.%). The maximum specific capacitance of the CCFs are 355 F g^{-1} at 1 A g^{-1} , 245.3 F g^{-1} at 0.8 A g^{-1} and 181.3 F g^{-1} at 0.2 A g^{-1} in KOH, H_2SO_4 and Na_2SO_4 electrolytes, respectively [33]. Du [20] et al. prepared activated carbon hollow fibers from cheap and renewable ramie fibers by ZnCl_2 activation. The activation temperature and activation time both have significant effect on the surface area, micropore volume and conductivity, further influence the electrochemical properties. A maximum capacity of 287 F g^{-1} at 50 mA g^{-1} was obtained under suitable conditions. Jin [21] et al. prepared activated carbon fibers from wood-derived fibers by melt-spinning process of mixture of waste wood shavings, phenol and phosphoric acid, curing and followed by a simple one-step process of carbonization and water vapor activation. The sample with optimal structure exhibits a high specific capacitance of 280 F g^{-1} at 0.5 A g^{-1} as well as excellent rate capability in $1 \text{ M H}_2\text{SO}_4$ and high capacitance retention of 99.3% over 2000 charge-discharge cycles.

In our previous reports, we prepared three-dimensional network like structured porous activated carbon by using willow catkins as raw materials and one-step KOH chemical activation process without pre-carbonization, the as-prepared activated carbon exhibited good electrochemical properties [34]. However, the original hollow fiber-like structure of willow catkins were destroyed seriously due to the KOH etching strongly, as a result, the obtained samples became power-like morphologies. So, how to maintain the original hollow fiber-like structure of willow catkins in the final samples appears to be very important. Herein, we report novel hollow activated carbon fibers from biomass willow catkins by a two-step process of pyrolysis and KOH activation. For contrast, the other two artificial HACFs were also fabricated by melt-spinning of high-molecular polymer phenolic resin and pitch, followed by pre-carbonization and KOH activation under the same process parameters. The morphology, pore structure, surface chemical composition and electrochemical properties of the samples were studied. The as-prepared willow catkins derived HACFs show unique high-hollow tubular structure, high microporous specific surface area ($1067 \text{ m}^2 \text{ g}^{-1}$), concentrated pore size distribution ($0.7 \sim 1.2 \text{ nm}$), abundant surface heteroatom-doped functional groups (2.39 wt.% N and 16.41 wt.% O species) and thus display excellent electrochemical performances in KOH aqueous electrolyte.

2. Experiments

2.1. Preparation of WCs derived HACFs

The preparation process of WCs derived HACFs was shown in Fig. 1. The WCs were cleaned with acetone and deionized water to remove the surface adherent impurities and dried at 80°C . The dried WCs were pyrolyzed at 500°C for 2 h under nitrogen flow with a heating rate of 5°C min^{-1} in horizontal tubular furnace to obtain hollow carbon fibers. Then, the hollow carbon fibers were mixed with KOH with the mass ratio of 1:1 and the mixture was treated at 700°C for 2 h under nitrogen flow with a heating rate of 5°C min^{-1} . After being cooled down to room temperature, the mixture was washed with 1 M HCl and deionized water alternately until the filtrate reached to neutral. The final samples were obtained after drying in vacuum at 80°C overnight and labeled as willow-HACFs.

2.2. Preparation of phenolic-based HACFs

The thermoplastic phenolic resin was used as raw material to prepare hollow phenolic fibers by melt spinning techniques with hollow spinneret at 150°C . Then, the obtained hollow phenolic fibers were cured in hexamethylenetetramine solution for 10 min, and pre-carbonized at 500°C for 2 h under nitrogen flow with a heating rate of 5°C min^{-1} in horizontal tubular furnace. Then, the phenolic derived hollow carbon fibers were mixed with KOH at mass ratio of 1:1 and pyrolyzed at 700°C for 2 h under nitrogen atmospheres at heating rate of 5°C min^{-1} . The ultimate samples were named as phenolic-HACFs.

2.3. Preparation of pitch-based HACFs

Similar to the preparation of phenolic-based HACFs, the pitch-based HACFs were fabricated by melt spinning techniques with isotropic pitch as raw material and the spinning temperature is 355°C followed by pre-oxidization at 300°C for 3 h and pyrolyzation at 500°C for 2 h. Then, the pitch-based hollow carbon fibers were mixed with KOH at mass ratio of 1:1 and heat-treated at 700°C for 2 h under nitrogen atmospheres at heating rate of 5°C min^{-1} . The final pitch derived hollow activated carbon fibers were denoted as pitch-HACFs.

2.4. Sample characterization

The microstructures and morphologies of the three kinds of HACFs were performed with field emission scanning electron microscopy (FE-SEM) on a JEOL JSM-7001F microscopy at an accelerating voltage of 10 kV. Nitrogen sorption isotherms and physical properties were examined by ASAP 2020 physisorption apparatus at 77K. The samples were degassed at 250°C for 5 h prior to the measurement. The surface area was calculated by Brunauer-Emmett-Teller (BET) method based on the nitrogen adsorption data in the P/P_0 range corresponding to linear region. The pore size distribution (PSD) was obtained by non-local density functional theory (NLDFT) method with an assumption of slit pore model [35]. X-ray photoelectron spectra (XPS) was measured on a Kratos AXIS Ultra DLD spectrometer with Al target, $\text{K}\alpha$ radiation, from a double anode X-ray source.

2.5. Electrochemical measurements

Both three-electrode and Two-electrode configurations were adopted to evaluate the capacitive properties of the as-prepared HACFs on a CHI 660C electrochemical workstation (Shanghai Chenhua Instruments Co., China). In three-electrode system, the

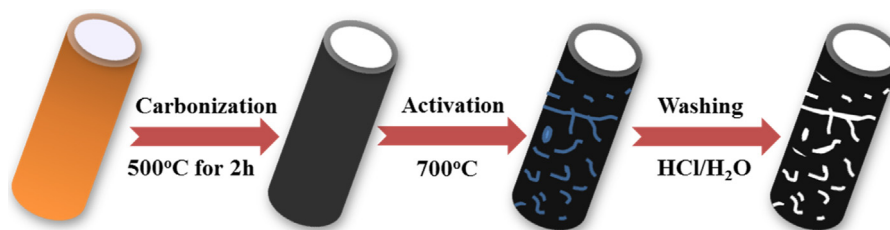


Fig. 1. Schematic illustration of preparation of willow catkins derived HACFs.

electrochemical properties of these HACFs were carried out in 6M KOH aqueous electrolytes solution, and a platinum foil and Hg/HgO electrode were used as the counter electrode and reference electrode, respectively. The working electrodes were prepared by mixing the activated materials, acetylene black, conducting graphite and polytetrafluoroethylene (PTFE) binder at a weight ratio of 75:10:10:5. A small amount of ethanol was added and the mixture was pestled by mortar to form an evenly slurry, the slurry were coated onto a nickel foam current collector and dried at 80 °C overnight in a vacuum and pressed at a pressure of 10 MPa. Cyclic voltammetry (CV) curves were obtained in potential range of $-0.9-0\text{ V}$ vs Hg/HgO by varying the scan rate from 5 to 200 mV s^{-1} . Charge-discharge measurements were carried out galvanostatically at $0.1-10\text{ A g}^{-1}$ over a voltage range of $-0.9-0\text{ V}$ vs Hg/HgO. Electrochemical impedance spectroscopy (EIS) was performed in a frequency range of 10 mHz–100 kHz at the open circuit voltage with alternate current amplitude of 5 mV. The specific capacitance of the three-electrode system was calculated using the following equation [36,37]:

$$C = \frac{I\Delta t}{m\Delta V} \quad (1)$$

Where C is the specific capacitance (F g^{-1}), I is the charge current (A), Δt is the discharge time (s), m is the mass of the active material in the electrode (g) and ΔV is the potential change in discharge (V).

The symmetric supercapacitor device was fabricated by separating two electrodes with a filter paper soaked with 6M KOH electrolyte and CR-2016 model battery jar were used as current collector. The cyclic voltammetry and galvanostatic charge-discharge tests of the electrochemical capacitor were performed in a two-electrode cell assembly. The specific capacitance of the two-electrode symmetrical supercapacitor cell was calculated using the follow equation [38,39]:

$$C_{\text{cell}} = \frac{I\Delta t}{m\Delta V} \quad (2)$$

where I is the discharge current (A), Δt is the discharge time (s), m is the total mass of anode and cathode materials (g) and ΔV is the potential change in discharge (V). The gravimetric capacitance of the carbon material electrode in the two-electrode system from galvanostatic charge-discharge was calculated using the formula [40]:

$$C_{\text{carbon}} = \frac{4I\Delta t}{m\Delta V} \quad (3)$$

The power and energy density were calculated based on the total mass of anode and cathode materials. Energy density was calculated using the following formula [41]:

$$E = \frac{C_{\text{cell}}V^2}{2} \quad (4)$$

where C_{cell} is the total cell specific capacitance (F g^{-1}) and V is the cell-operation potential (V). The average power density was obtained by using the following formula:

$$P = \frac{E}{\Delta t} \quad (5)$$

where E is the energy density and Δt is the discharge time.

3. Results and discussion

3.1. SEM analysis

Fig. 2 depicted the microstructure images of the three kinds of HACFs. Under low-resolution SEM observations, all HACFs had a hollow fibrous structure, but different hollowness. Fig. 2a,b are the SEM images of willow catkins based HACFs under low and high magnifications, respectively. It indicates that after activation, most hollow fibers retain the hollow microstructure of original willow catkins [34]. The tubular diameter is less than $10\text{ }\mu\text{m}$, and the thickness of the tube wall is obviously less than that of the phenolic-based and pitch-based HACFs. From the Fig.S1, it can also be observed that O and N elements were uniformly distributed in the willow-based carbon skeleton, demonstrating the co-existence of oxygen- and nitrogen-containing functional groups. Active oxygen- and nitrogen-containing functional groups can not only enhance the effective contact area between the electrode materials and aqueous electrolyte by improving the wettability, but also provide rich active sites for the fast redox reaction. Fig. 2c, d also show the SEM images of phenolic-based HACFs under low and high magnifications, respectively, due to the limitation of the spinning equipments and process conditions, the hollowness of phenolic-based HACFs is relatively low and the tube wall is thicker. After KOH activation, although the tube walls were seriously etched, the phenolic-based HACFs still maintain intact hollow fiber structure while the tube wall is unbroken. However, for pitch-based HACFs (Fig. 2e, f), the hollowness is also lower than that of the willow catkins based HACFs. Besides, due to the high contents of aromatic constituents, it is more likely to form well-organized carbon crystallite structure with a higher degree of graphitization than the willow catkins based HACFs and phenolic based HACFs. After activation process, the resulting activated samples show less defects, more smoother surface and lower porosity.

3.2. Surface area and pore size analysis

All samples depicted typical characteristic of Type-I-nitrogen adsorption-desorption isotherms (Fig. 3a). A steep increase at the low relative pressure ($P/P_0 < 0.05$) and a fairly flat plateau in the high pressure implies that the samples are predominant microporous. Besides, the willow-HACFs have apparent H4 hysteresis loops from a capillary condensation step at relatively high pressure ($P/P_0 = 0.45 \sim 1.0$), demonstrating the existence of mesopores [42,43]. The pore structure parameters of all samples are listed in Table 1. The specific surface area (SSA) of willow-HACFs, phenolic-HACFs and pitch-HACFs are 1115, 1327, $286\text{ m}^2\text{ g}^{-1}$, respectively.

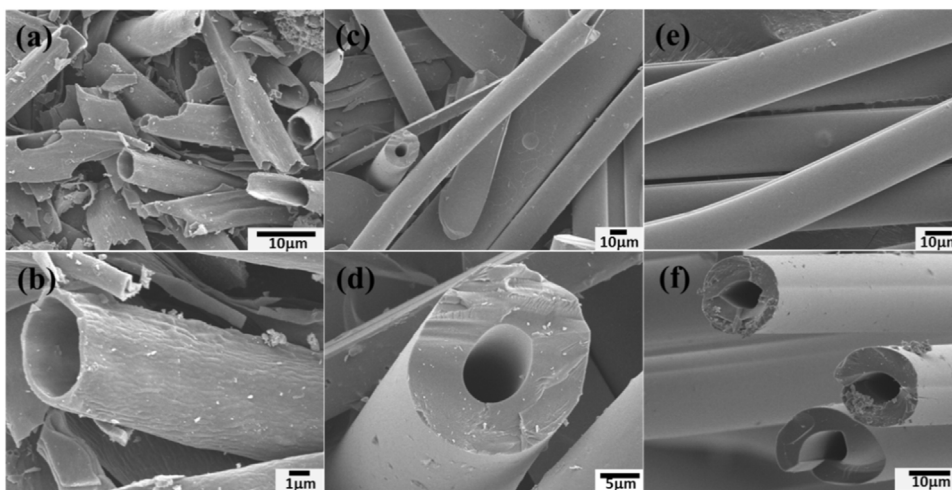


Fig. 2. (a)(b) SEM images of willow-HACFs; (c)(d) SEM images of phenolic-HACFs; (e)(f) SEM images of pitch-HACFs.

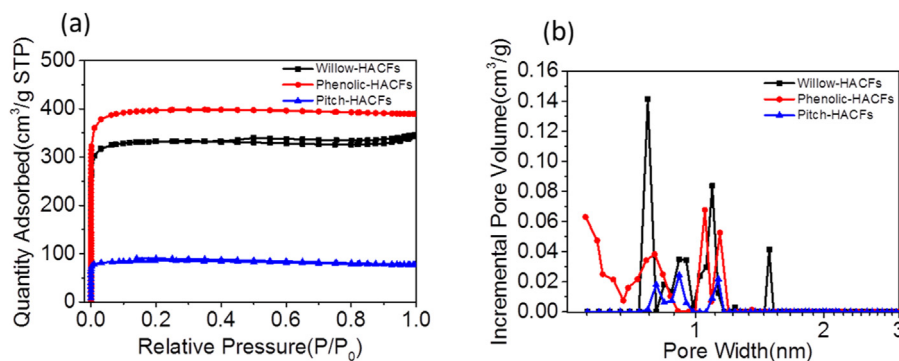


Fig. 3. (a) Nitrogen adsorption-desorption isotherms; (b) pores size distribution curves.

Table 1
The pore structure properties of samples.

Samples	S_{BET} $\text{m}^2 \text{g}^{-1}$	S_{micro} $\text{m}^2 \text{g}^{-1}$	V_{total} $\text{cm}^3 \text{g}^{-1}$	V_{micro} $\text{cm}^3 \text{g}^{-1}$	$V_{0.7-1.2}$ $\text{cm}^3 \text{g}^{-1}$
Willow-HACFs	1115	1067	0.53	0.49	0.394
Phenolic-HACFs	1327	1242	0.60	0.56	0.257
Pitch-HACFs	286	275	0.12	0.118	0.095

S_{BET} is the specific surface area measured by BET method. S_{micro} is micropore surface area calculated by t-plot method. V_{total} is total pore volume measured at $P/P_0 = 0.995$. V_{micro} is micropore volume obtained by t-plot method. $V_{0.7-1.2}$ is micropore volume of the pore with diameter between 0.7 and 1.2 nm.

The three samples were mainly composed of micropores, which was greatly related to the KOH activation process. The activation mechanisms for the KOH activation of carbon have been widely studied [1,44,45]. When the activation temperature below 700 °C, the carbon framework is etched by the redox reactions between carbon and various potassium compounds (KOH, K_2CO_3 and K_2O), which are responsible for the creating of porous microstructure. Moreover, the porosity is further developed through the gasification of carbon to CO, which is ascribed to the consumption of carbon by H_2O and CO_2 generated during the activation process. At temperature above 700 °C, potassium compound (K_2CO_3 and K_2O) are reduced to metallic K by carbon, and this metallic K could efficiently intercalate into the lattices of carbon skeleton during the activation process. Therefore, the carbon lattices are irreversibly expanded. The intercalated K and other K compounds will be removed by subsequently expanded, which also results in the formation of amorphous and porous structures containing numerous micropores

and small amounts of mesopores. Fig. 3b gives the pores size distribution curves. All the samples show relatively narrow pores size distribution and mainly concentrated at 0.7 ~ 1.2 nm. Interestingly, the willow-HACFs possess the highest micropore volume at pore diameter between 0.7 and 1.2 nm (as shown in Table 1), which is especially favorable for energy storage of electric double layer capacitor (EDLC).

3.3. XPS analysis

Surface chemical compositions of samples were measured by X-ray photoelectron spectroscopy (XPS). The weak signal at the binding energy of 400 eV assigned to N 1s and pronounced signal at 532 eV ascribed to O 1s (Fig. 4a) demonstrate that the three kinds of HACFs are rich in surface active oxygen-containing functional groups, and contain small amounts of active nitrogen-containing functional groups. The O 1s region spectrum can be mainly deconvoluted into four peaks, which are corresponding to four types of oxygen functional groups (Fig. 4b): 531.4 ± 0.2 eV attributed to carbonyl (C=O) and/or quinone (marked as O-I); 532.3 ± 0.2 eV assigned to hydroxyl (C–OH) and ether (C–O–C) (marked as O-II); 533.3 ± 0.3 eV ascribed to carboxyl (COO^-) (marked as O-III) as well as 535.9 ± 0.4 eV due to chemisorbed oxygen and/or water (marked as O-IV) [46,47]. The total oxygen contents of three samples are 16.41, 9.61, 12.23 wt.%, respectively (Table 2). The willow-HACFs have the highest contents of oxygen. Basic oxygen groups (O-I and O-II) are supposed to be electrochemical redox activity, and considered beneficial to pseudocapacitance [48]. The total quantity of O-I and O-II of the three samples are 6.32, 7.21 and

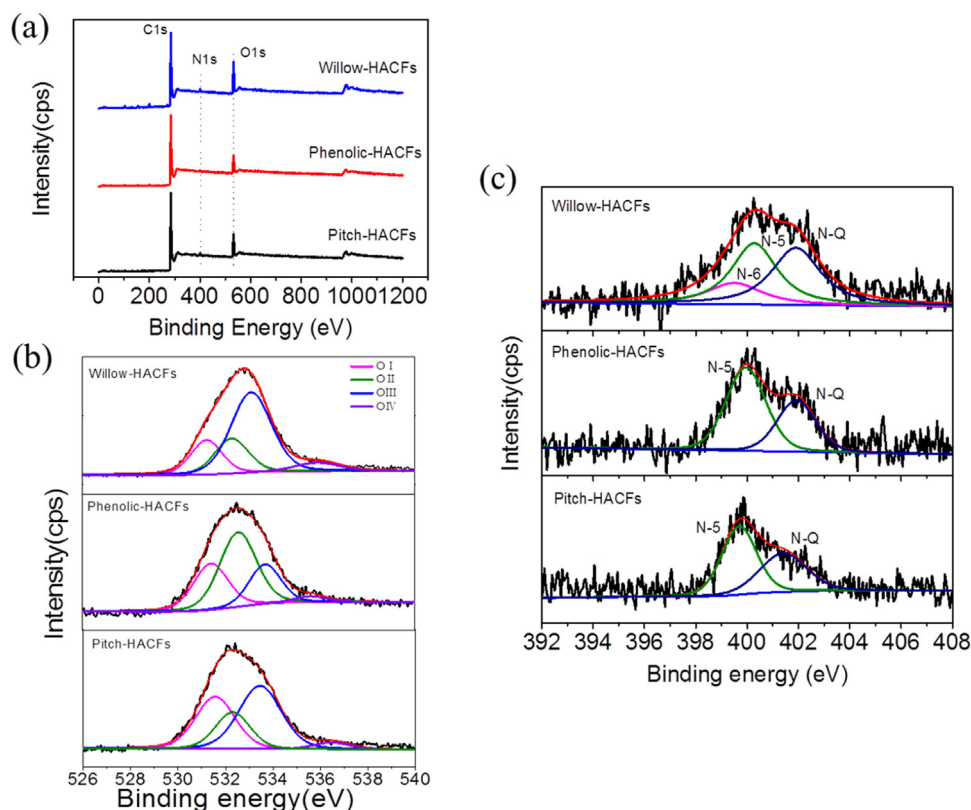


Fig. 4. (a) XPS survey spectra, High-resolution XPS spectra of (b) the deconvoluted O 1s peak and (c) N 1s peak.

Table 2
Elemental composition and surface functional groups of samples.

Samples	C wt.%	N wt.%	O wt.%	N5 wt.%	N6 wt.%	NQ wt.%	OI wt.%	OII wt.%	OIII wt.%	OIV wt.%
willow	81.2	2.39	16.41	0.9	0.31	1.18	3.01	3.31	9.02	1.07
phenolic	89.29	1.10	9.61	0.69	–	0.41	2.67	4.54	2.08	0.33
pitch	86.15	1.62	12.23	0.92	–	0.70	4.0	2.49	5.25	0.49

6.49 wt.%, respectively, demonstrating the close contents of active oxygen functional groups. Fig. 4c depicts the deconvolutions of N 1s region spectrum that identify the surface nitrogen-containing functional groups. For the willow-HACFs, pyridinic (N-6, 399.4 eV), pyrrolic and/or pyridonic (N-5, 400.3 eV) and quaternary nitrogen (N-Q, 401.9 eV) [49,50] are observed. However, for the phenolic-HACFs, due to the introduction of small amounts of nitrogen element during the curing process of hexamethylenetetramine, the peaks at 399.9 and 401.8 eV are correspond to N-5 and N-Q, respectively. While the small amount of nitrogen contents in the pitch lead to less active nitrogen functional groups of the pitch-HACFs. Based on the previous reports on active nitrogen functional groups, in generally, the exposed N-6 and N-5 in the edge of graphite could improve the electron donor/receptor, further affect the charge-discharge behavior of supercapacitor, providing the pseudocapacitance [51]. However, although the nitrogen functionalities locating at the middle of graphite (N-Q) are found generally less active, they can greatly improve the conductivity of carbon materials [52]. Besides, when compared with phenolic-HACFs and pitch-HACFs, the willow-HACFs own the highest content of active nitrogen-containing functional group of 1.21 wt.%, which also greatly improve the electrochemical properties.

3.4. Electrochemical analysis

Fig. 5 gives the cyclic voltametry (CV) curves under the same scan rates for the three samples. At scan rate of 5 mV s^{-1} , the CV curves of all samples maintain good rectangular-like shape with obvious hump at low potential region, indicating the combination effects of electric double-layer capacitance (EDLC) and pseudocapacitance (oxidation or reduction reaction) result from the active nitrogen and/or oxygen heteroatoms [2,53]. With the increase of scan rate (Fig. 5b–d), the transmission rate of electric charges and electrolyte ions between the electrolytes and electrode materials increased, and the faster the scan rate, the more obvious distortion of the rectangular-like shape. This is mainly due to that in the mesopores and macropores, the moving resistance of electrolyte ions is relatively low, but in micropores, the moving resistance of electrolyte ions is high. For the three kinds of HACFs, they are primarily constituted of micropores. Therefore, the higher scan rate increased the transfer resistance of electrolyte ions that make it difficult to fulfill the charge transfer instantaneously. As a result, the CV curves distort seriously. Moreover, the willow-HACFs exhibit the largest area of loop at the same scan rate, suggesting the highest capacitance among them.

Fig. 6a gives the GCD curves of the samples at low current density of 0.1 A g^{-1} . The GCD curves show that the charge and discharge curves have preferable symmetry, demonstrating the good electrochemical reversibility [54,55]. The inflections at $\sim 0.2 \text{ V}$ of the samples imply the impact of pseudocapacitance due to the effect of active functional groups. At relative high current density of 5 A g^{-1} (as shown in Fig. 6b), the GCD curves still retain almost symmetrical and obvious IR drops are observed. The value of IR drops are 0.07, 0.071 and 0.12 V for the willow-HACFs, phenolic-HACFs and pitch-HACFs, respectively. It is indicated that the willow-HACFs based electrode shows the lowest resistance and good conduc-

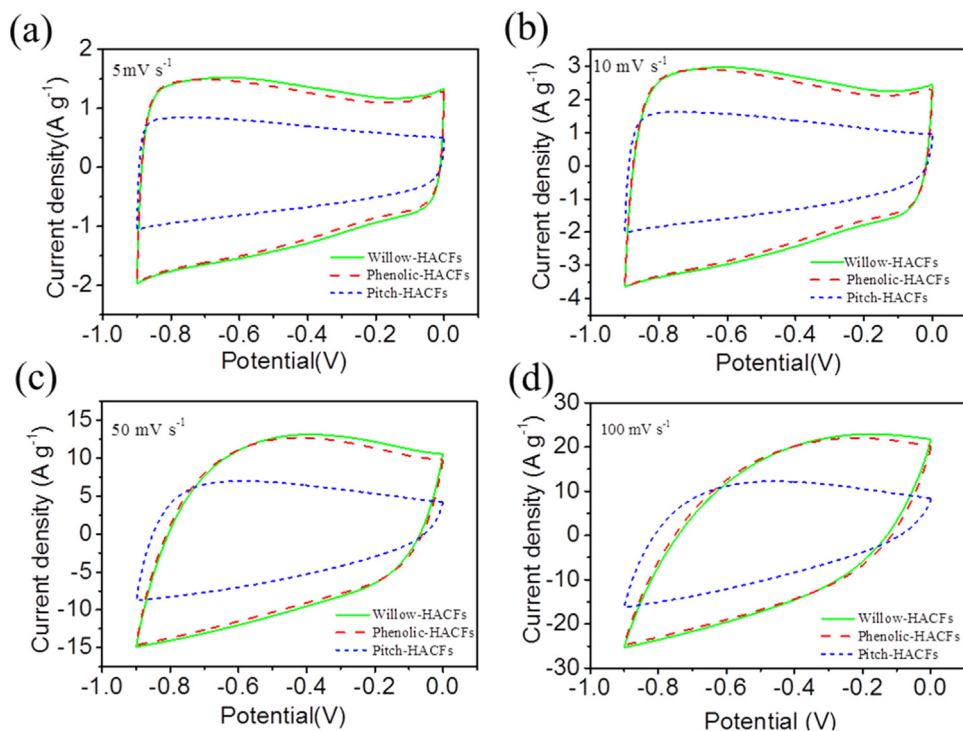


Fig. 5. CV curves of samples at scan rates of (a) 5 mV s^{-1} ; (b) 10 mV s^{-1} ; (c) 50 mV s^{-1} ; (d) 100 mV s^{-1} .

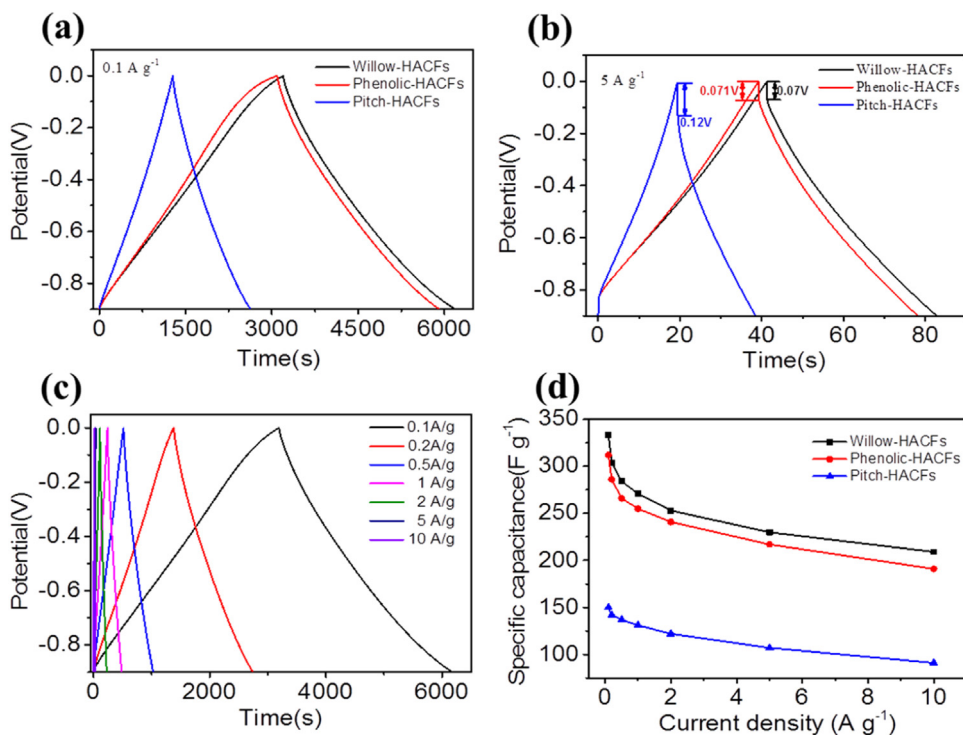


Fig. 6. (a) GCD curves of all samples at 0.1 A g^{-1} ; (b) at 5 A g^{-1} ; (c) GCD curves of willow-HACFs at different current densities ($0.1\text{--}10 \text{ A g}^{-1}$); (d) the dependence of the capacitance of all samples as a function of current density.

tivity, thus has better power performance. Fig. 6c exhibits the GCD curves of willow-HACFs at increased current densities ranging from 0.1 to 10 A g^{-1} , which is a typical characteristic of an ideal capacitor with good electrochemical reversibility. Based on the galvanostatic discharge curves, the specific capacitances of electrode

materials are calculated by Eq. (1) and the results are showed in Fig. 6d. At low current density of 0.1 A g^{-1} , the specific capacitance of willow-HACFs, phenolic-HACFs and pitch-HACFs electrodes are 333 , 312 and 150 F g^{-1} , respectively. The specific capacitance of electrode materials all decreased with the increase of current den-

sity due to the combination of electrode resistance and electrolyte transfer resistance. At high current density of 10 A g^{-1} , the specific capacitance of electrode materials are 209, 191 and 91 F g^{-1} , corresponding to the capacitive retention rate of 62.7%, 61.2% and 60.7%, respectively. It can be concluded that the willow-HACFs based electrodes have the somewhat better capacitive performance and rate capability.

Fig. 7a provides the AC impedance spectra, which shows that all samples exhibit typical characteristic of porous carbon electrodes. At high frequency region, the real part of resistance (Z') such as the intercept of plot with real axis that stands for the equivalent series resistance (ESR) R_s , which is a combination of ionic resistance of the electrolyte, the intrinsic resistance of the electrode materials and contact resistance between the electrode materials and current collector. The R_s value are 0.8, 0.7 and 0.68Ω for the willow-HACFs, phenolic-HACFs and pitch-HACFs, respectively. At medium-high frequency region, an obvious semicircle loop is observed, which represents the charge transfer resistance (R_{ct}) at the interface between the electrode and electrolytes, as shown in the inset of the magnified high-frequency region of Fig. 7a. The small semicircle of the willow-HACFs (about 0.4Ω) is nearly the same as that of the phenolic-HACFs, much less than that of the pitch-HACFs (almost 4.0Ω), demonstrating the good ionic conductivity of the willow-HACFs based electrode materials. All the samples display good capacitive behavior with nearly vertical slope at low frequency region, and the larger slope of the willow-HACFs indicates the excellent capacitive performance. Fig. 7b–d show the plots of bode phase angle with frequency of the three samples. The frequency at 45° corresponding to the characteristic frequency f_0 of capacitor, represents the transfer frequency from resistance behavior to capacitive behavior. The relaxation time τ_0 is calculated by $\tau_0 = 1/f_0$. From the characteristic frequency of the samples, the value of τ_0 are 7.7, 8.3 and 9.1 s, respectively. It is indicates that the sample of willow-HACFs own the faster ion response rate due to the

well-developed hollow structure and wider pore size distribution that decrease the ionic transfer resistance.

Fig. S2 show the GCD curve of the samples in the two-electrode system. Similar to the three-electrode system, the GCD curves of the symmetric supercapacitor in 6 M KOH aqueous electrolytes are almost symmetrical and linear at increased current densities, exhibiting good electrochemical reversibility. The pitch-HACFs derived symmetric supercapacitor shows apparent IR drop during the transition process of galvanostatic charge and discharge, also illustrating the large resistance of pitch-HACFs based electrode materials. Fig. S2d gives the relationship between specific capacitances and current densities. The specific capacitance decreased gradually with the increasing of current density. At current density of 0.1 A g^{-1} , the specific capacitance of supercapacitive electrode materials are 253, 201 and 86 F g^{-1} , respectively. While at high current density of 10 A g^{-1} , the willow-HACFs based electrode still maintain considerable specific capacitance of 143 F g^{-1} , indicating good rate performance in symmetric supercapacitor devices.

Fig. S3 also gives the CV curves of willow-HACFs, phenolic-HACFs and pitch-HACFs based electrode materials in symmetric supercapacitor. At the same current density, the sample of willow-HACFs has the highest current density and largest area of loop, which indicates the highest specific capacitance that is consistent with the GCD test result. When the scan rate increased from 5 to 200 mV s^{-1} , the CV curves of willow-HACFs and phenolic-HACFs based symmetric supercapacitor maintain good rectangular-like shape, which means the good capacitive behavior and rate performance. However, the CV curves of pitch-HACFs based symmetric supercapacitor distort from rectangular-like shape at low scan rate to spindle-like shape over 50 mV s^{-1} , indicating larger ionic transfer resistance and slower ionic response rate at higher scan rate.

Power density and energy density are two important factors on evaluating the energy storage performances of electrochemical storage devices. Fig. 8a shows the ragone curves of the three samples, the energy density of willow-HACFs based symmet-

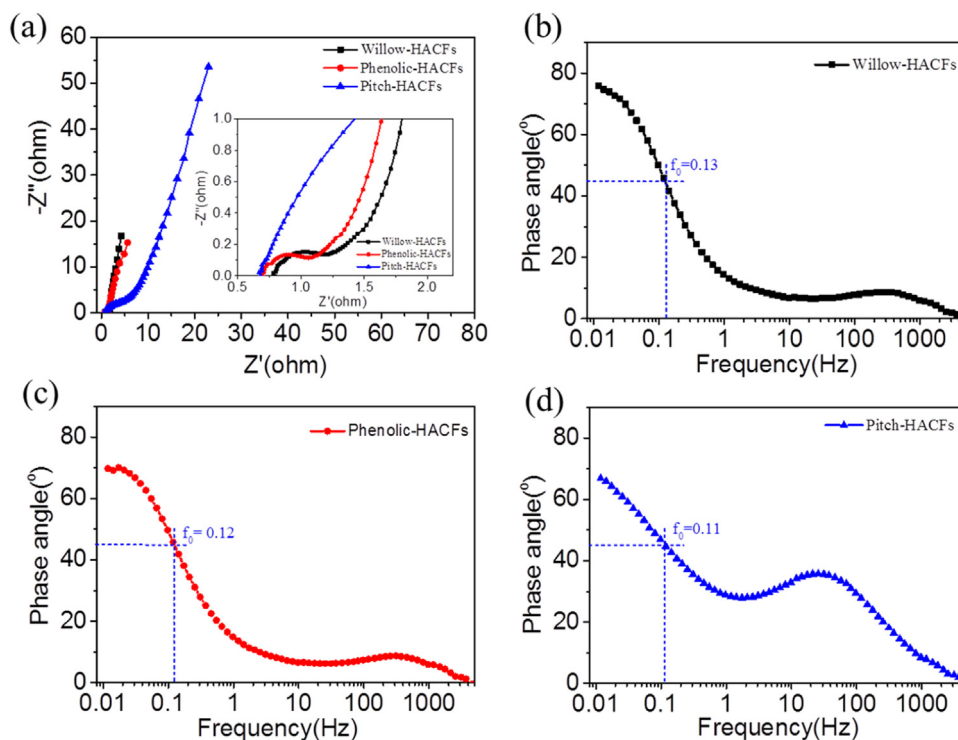


Fig. 7. (a) Nyquist plots of the samples; the inset shows the magnified view of the high-frequency region. (b) willow-HACFs; (c) phenolic-HACFs; (d) pitch-HACFs plot of Bode phase angle with frequency.

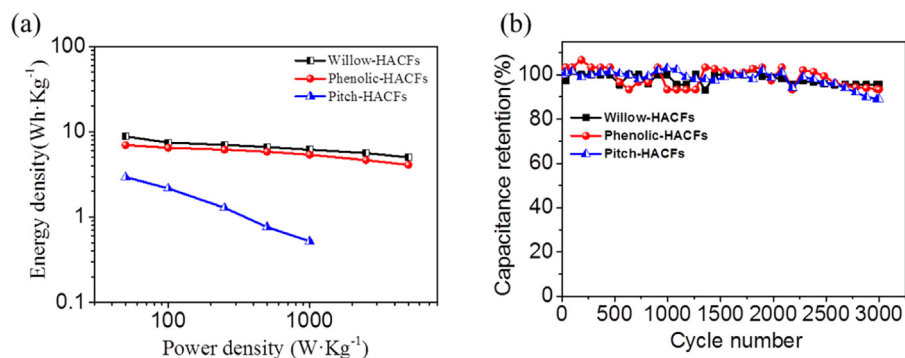


Fig. 8. (a) Ragone curves of samples; (b) Capacitance retention of samples with cycle number.

ric supercapacitor is 8.8 Wh kg⁻¹ at power density of 50 W kg⁻¹, higher than that of phenolic-HACFs based symmetric supercapacitor (7.0 Wh kg⁻¹) and pitch-HACFs based symmetric supercapacitor (3.0 Wh kg⁻¹). When the power density increased to 5000 W kg⁻¹, the willow-HACFs based symmetric supercapacitor still maintain appreciable energy density of 5.0 Wh kg⁻¹. Fig. 8b shows the variation of capacitance retention as a function of cycle number for the three samples at a current density of 5 A g⁻¹. It can be seen that after 3000 cycles, the capacitance retentions of willow-HACFs, phenolic-HACFs and pitch-HACFs are 95.5%, 93.3% and 89.1%, respectively. The active heteroatoms functionalities might be decayed and deactivated during the cycle process which may results in the attenuation of the capacitance retention. The N-Q functional groups can not only enhance the electric conductivity of carbon materials, but also improve the wettability between electrodes materials and electrolyte ions. As a result, the willow-HACFs based electrode materials with the highest contents of N-Q functional groups of 1.18 wt.% (Table 2) is favorable for the cycle stability of supercapacitor. Besides, the willow-HACFs possess more concentrated pore size distribution, while the phenolic-HACFs contain more micropores with pore size smaller than 0.7 nm which can not be store charges. So the willow-HACFs electrodes have higher charge storage efficiency which result in higher specific capacitance as well as better cycle stability.

Based on the above results, the following aspects may contribute to the good electrochemical performances of the as-prepared willow-HACFs. Firstly, the high SSA with abundant micropores concentrated at 0.7–1.2 nm is favorable for improving electrolyte contact and accumulating more electrolyte ions, and thus enhances the charge storage density. Secondly, the willow-HACFs have hollow tubular architecture with high hollowness and rough surface. This unique structure may store more electrolyte ions and reduce the transport distance of an electrolyte ion inside the micropores during the charge/discharge processes, resulting in excellent cycling stability and good rate capability. Thirdly, the higher content of nitrogen-doping and oxygen-containing functional groups can improve the wettability while more N-Q functional groups is helpful for enhancing the electrical conductivity of the willow-HACFs based electrodes, thus offering minimized diffusive resistance for the electrolyte ion transportation. Above all, a combination of the high SSA with concentrated micropores at 0.7–1.2 nm, the unique high-hollow tubular structures and the favorable nitrogen-doping functional groups synergistically lead to the extraordinary electrochemical performance for the willow-HACFs.

4. Conclusion

In brief, three different kinds of hollow activated carbon fibers (HACFs) derived from biomass willow catkins (WCs), phenolic- and pitch-based hollow fibers were fabricated, respectively. The

advantages of the specific high-hollow tubular structure, low-cost and renewability of nature biomass WCs compared to the melt-spun hollow fibers which make the willow-HACFs favorable in the preparation of electrode materials. The willow-HACFs possess high microporous specific surface area (1067 m² g⁻¹), more concentrated pore size distribution (0.7–1.2 nm), abundant surface heteroatom-doped functional groups (2.39 wt.% N and 16.41 wt.% O species) which results in excellent electrochemical properties due to the combination of EDLCs and pseudocapacitance. Electrochemical measurements show that the WCs derived HACFs not only exhibit a high specific capacitance of 333 F g⁻¹ at 0.1 A g⁻¹ but also show considerable rate capability with a retention of 62.7% (209 F g⁻¹ at 10 A g⁻¹). Furthermore, as-fabricated willow-HACFs based symmetric supercapacitor device delivers a maximum energy density of ~8.8 Wh kg⁻¹ at power density of 50 W kg⁻¹ as well as good cycling performance with 95.5% retention over 3000 cycles at 5 A g⁻¹ in 6 M KOH aqueous electrolytes. The outstanding electrochemical performance of the supercapacitor device makes it promising to use in a high-performance electrochemical energy system.

Acknowledgments

This work was financially supported by the Natural Science Foundation of Shanxi Province (No. 2012011219-3) and Youth Innovation Promotion Association CAS.

Appendix A. Supplementary data

Supplementary data associated with this article can be found, in the online version, at <http://dx.doi.org/10.1016/j.apsusc.2016.10.161>.

References

- [1] Y. Zhu, S. Murali, M.D. Stoller, K.J. Ganesh, W. Cai, P.J. Ferreira, et al., Carbon-based supercapacitors produced by activation of graphene, *Science* 322 (2011) 1537–1541.
- [2] L. Zhao, L.-Z. Fan, M.-Q. Zhou, H. Guan, S. Qiao, M. Antonietti, et al., Nitrogen-containing hydrothermal carbons with superior performance in supercapacitors, *Adv. Mater.* 225 (2010) 202–206.
- [3] J. Yan, Q. Wang, T. Wei, Z. Fan, Recent advances in design and fabrication of electrochemical supercapacitors with high energy densities, *Adv. Energy Mater.* 4 (2014) 1–43.
- [4] L.L. Zhang, X.S. Zhao, Carbon-based materials as supercapacitor electrodes, *Chem. Soc. Rev.* 38 (2009) 2520–2531.
- [5] X. Lu, M. Yu, G. Wang, Y. Tong, Y. Li, Flexible solid-state supercapacitors: design: fabrication and applications, *Energy Environ. Sci.* 7 (2014) 2160–2181.
- [6] C. Xu, B. Xu, Y. Gu, Z. Xiong, J. Sun, X.S. Zhao, Graphene-based electrodes for electrochemical energy storage, *Energy Environ. Sci.* 6 (2013) 1388–1414.
- [7] H. Zhu, X. Wang, F. Yang, X. Yang, Promising carbons for supercapacitors derived from fungi, *Adv. Mater.* 23 (2011) 2745–2748.

- [8] Q. Wang, J. Yan, Z. Fan, Carbon materials for high volumetric performance supercapacitors: design progress, challenges and opportunities, *Energy Environ. Sci.* 9 (2016) 729–762.
- [9] Y.-Q. Zhao, M. Lu, P.-Y. Tao, Y.-J. Zhang, X.-T. Gong, Z. Yang, et al., Hierarchically porous and heteroatom doped carbon derived from tobacco rods for supercapacitors, *J. Power Sources* 307 (2016) 391–400.
- [10] Z. Yu, L. Tetard, L. Zhai, J. Thomas, Supercapacitor electrode materials: nanostructures from 0 to 3 dimensions, *Energy Environ. Sci.* 8 (2015) 702–730.
- [11] H. Nakagawa, A. Shudo, K. Miura, High capacity electric double layer capacitor with high density activated carbon fiber electrodes, *J. Electrochem. Soc.* 147 (2000) 38–42.
- [12] J.-G. Lee, J.-Y. Kim, S.-H. Kim, Effects of microporosity on the specific capacitance of polyacrylonitrile-based activated carbon fiber, *J. Power Sources* 160 (2006) 1495–1500.
- [13] K. Wang, R. Yan, N. Zhao, X. Tian, X. Li, S. Lei, et al., Bio-inspired hollow activated carbon microtubes derived from willow catkins for supercapacitors with high volumetric performance, *Mater. Lett.* 174 (2016) 249–252.
- [14] L. Sun, C. Tian, M. Li, X. Meng, L. Wang, R. Wang, et al., From coconut shell to porous graphene-like nanosheets for high-power supercapacitors, *J. Mater. Chem. A* 1 (2013) 6462–6470.
- [15] H. Peng, G. Ma, K. Sun, J. Mu, Z. Lei, One-step preparation of ultrathin nitrogen-doped carbon nanosheets with ultrahigh pore volume for high-performance supercapacitors, *J. Mater. Chem. A* 2 (2014) 17297–17301.
- [16] P.A. Goodman, H. Li, Y. Gao, Y.F. Lu, J.D. Stenger-Smith, J. Redepenning, Preparation and characterization of high surface area: high porosity carbon monoliths from pyrolyzed bovine bone and their performance as supercapacitor electrodes, *Carbon* 55 (2013) 291–298.
- [17] X.-L. Wu, T. Wen, H.-L. Guo, S. Yang, X. Wang, A.-W. Xu, Biomass-derived sponge-like carbonaceous hydrogels and aerogels for supercapacitors, *ACS Nano* 7 (2013) 3589–3597.
- [18] A.B. Fuertes, G.A. Ferrero, M. Sevilla, One-pot synthesis of microporous carbons highly enriched in nitrogen and their electrochemical performance, *J. Mater. Chem. A* 2 (2014) 14439–14448.
- [19] T.E. Rufford, D. Hulicova-Jurcakova, Z. Zhu, G.-Q. Lu, Empirical analysis of the contributions of mesopores and micropores to the double-layer capacitance of carbons, *J. Phys. Chem. C* 113 (2009) 19335–19343.
- [20] X. Du, W. Zhao, Y. Wang, C. Wang, M. Chen, T. Qi, et al., Preparation of activated carbon hollow fibers from ramie at low temperature for electric double-layer capacitor applications, *Bioresour. Technol.* 149 (2013) 31–37.
- [21] Z. Jin, X. Yan, Y. Yu, G. Zhao, Sustainable activated carbon fibers from liquefied wood with controllable porosity for high-performance supercapacitors, *J. Mater. Chem. A* 2 (2014) 11706–11715.
- [22] Y.M. Chen, Z. Li, X.W. Lou, General formation of $M_x\text{Co}_{3-x}\text{S}_4$ (Mn, Mn: Zn) hollow tubular structures for hybrid supercapacitors, *Angew Chem. Int. Ed.* 127 (2015) 1–5.
- [23] Y. Yin, R.M. Rioux, C.K. Erdonmez, S. Hughes, G.A. Somorjai, A.P. Alivisatos, Formation of hollow nanocrystals through the nanoscale kirkendall effect, *Science* 304 (2004) 711–714.
- [24] B.Y. Xia, H.B. Wu, X. Wang, X.W. Lou, One-pot synthesis of cubic PtCu_3 nanocages with enhanced electrocatalytic activity for the methanol oxidation reaction, *J. Am. Chem. Soc.* 134 (2012) 13934–13937.
- [25] Y. Zhu, J. Shi, W. Shen, X. Dong, J. Feng, M. Ruan, et al., Stimuli-responsive controlled drug release from a hollow mesoporous silica sphere/polyelectrolyte multilayer Core-shell structure, *Angew Chem. Int. Ed.* 44 (2005) 5083–5087.
- [26] J. Liu, S.Z. Qiao, J.S. Chen, X.W. Lou, X. Xing, G.Q. Lu, Yolk/shell nanoparticles: new platforms for nanoreactors: drug delivery and lithium-ion batteries, *Chem. Commun.* 47 (2011) 12578–12591.
- [27] L. Yu, H.B. Wu, X.W. Lou, Mesoporous $\text{Li}_4\text{Ti}_5\text{O}_{12}$ hollow spheres with enhanced lithium storage capability, *Adv. Mater.* 25 (2013) 2296–2300.
- [28] J. Nai, Y. Tian, X. Guan, L. Guo, Pearson's principle inspired generalized strategy for the fabrication of metal hydroxide and oxide nanocages, *J. Am. Chem. Soc.* 135 (2013) 16082–16091.
- [29] M. Ibáñez, A. Cabot, All change for nanocrystals, *Science* 340 (2013) 935–936.
- [30] E. Raymundo-Piñero, M. Cadek, F. Béguin, Tuning carbon materials for supercapacitors by direct pyrolysis of seaweeds, *Adv. Funct. Mater.* 19 (2009) 1032–1039.
- [31] J. Deng, Y. You, V. Sahajwalla, R.K. Joshi, Transforming waste into carbon-based nanomaterials, *Carbon* 96 (2016) 105–115.
- [32] K.R. Saravanan, N. Kalaiselvi, Nitrogen containing bio-carbon as a potential anode for lithium batteries, *Carbon* 81 (2015) 43–53.
- [33] S. Wang, Z. Ren, J. Li, Y. Ren, L. Zhao, J. Yu, Cotton-based hollow carbon fibers with high specific surface area prepared by ammonia etching for supercapacitor application, *RSC Adv.* 4 (2014) 31300–31307.
- [34] K. Wang, N. Zhao, S. Lei, R. Yan, X. Tian, J. Wang, et al., Promising biomass-based activated carbons derived from willow catkins for high performance supercapacitors, *Electrochim. Acta* 166 (2015) 1–11.
- [35] J. Song, W. Shen, J. Wang, W. Fan, Superior carbon-based CO_2 adsorbents prepared from poplar anthers, *Carbon* 69 (2014) 255–263.
- [36] A. Alabadi, X. Yang, Z. Dong, Z. Li, B. Tan, Nitrogen-doped activated carbons derived from a co-polymer for high supercapacitor performance, *J. Mater. Chem. A* 2 (2014) 11697–11705.
- [37] Y. Fan, X. Yang, B. Zhu, P.-F. Liu, H.-T. Lu, Micro-mesoporous carbon spheres derived from carrageenan as electrode material for supercapacitors, *J. Power Sources* 268 (2014) 584–590.
- [38] Z. Lei, N. Christov, X.S. Zhao, Intercalation of mesoporous carbon spheres between reduced graphene oxide sheets for preparing high-rate supercapacitor electrodes, *Energy Environ. Sci.* 4 (2011) 1866–1873.
- [39] B. Li, F. Dai, Q. Xiao, L. Yang, J. Shen, C. Zhang, et al., Nitrogen-doped activated carbon for a high energy hybrid supercapacitor, *Energy Environ. Sci.* 9 (2016) 102–106.
- [40] C.-M. Chen, L. Xie, G. Sun, F. Su, Q.-Q. Kong, X. Guo, et al., Hierarchical porous carbon microtubes derived from willow catkins for supercapacitor application, *J. Mater. Chem. A* 4 (2016) 1637–1646.
- [41] M. Biswal, A. Banerjee, M. Deo, S. Ogale, From dead leaves to high energy density supercapacitors, *Energy Environ. Sci.* 6 (2013) 1249–1259.
- [42] F.L. Braghioroli, V. Fierro, A. Szczurek, N. Stein, J. Parmentier, A. Celzard, Hydrothermally treated aminated tannin as precursor of N-doped carbon gels for supercapacitors, *Carbon* 90 (2015) 63–74.
- [43] T. Kim, G. Jung, S. Yoo, K.S. Suh, R.S. Ruoff, Activated graphene-based carbons as supercapacitor electrodes with macro- and mesopores, *ACS Nano* 7 (2013) 6899–6905.
- [44] M.A. Lillo-Ródenas, D. Cazorla-Amorós, A. Linares-Solano, Understanding chemical reactions between carbons and NaOH and KOH: An insight into the chemical activation mechanism, *Carbon* 41 (2003) 267–275.
- [45] J. Wang, S. Kaskel, KOH activation of carbon-based materials for energy storage, *J. Mater. Chem.* 22 (2012) 23710–23725.
- [46] X. Tian, N. Zhao, Y. Song, K. Wang, D. Xu, X. Li, et al., Synthesis of nitrogen-doped electrospun carbon nanofibers with superior performance as efficient supercapacitor electrodes in alkaline solution, *Electrochim. Acta* 185 (2015) 40–51.
- [47] C. Ma, Y. Li, J. Shi, Y. Song, L. Liu, High-performance supercapacitor electrodes based on porous flexible carbon nanofiber paper treated by surface chemical etching, *Chem. Eng. J.* 249 (2014) 216–225.
- [48] C. Wang, Y. Zhou, L. Sun, P. Wan, X. Zhang, J. Qiu, Sustainable synthesis of phosphorus- and nitrogen-co-doped porous carbons with tunable surface properties for supercapacitors, *J. Power Sources* 239 (2013) 81–88.
- [49] B. Xu, S. Hou, G. Cao, F. Wu, Y. Yang, Sustainable nitrogen-doped porous carbon with high surface areas prepared from gelatin for supercapacitors, *J. Mater. Chem.* 22 (2012) 19088–19093.
- [50] Z. Li, Z. Xu, X. Tan, H. Wang, C.M.B. Holt, T. Stephenson, et al., Mesoporous nitrogen-rich carbons derived from protein for ultra-high capacity battery anodes and supercapacitors, *Energy Environ. Sci.* 6 (2013) 871–878.
- [51] D. Hulicova-Jurcakova, M. Seredych, G.Q. Lu, T.J. Bandoz, Combined effect of nitrogen- and oxygen-containing functional groups of microporous activated carbon on its electrochemical performance in supercapacitors, *Adv. Funct. Mater.* 19 (2009) 438–447.
- [52] C.O. Ania, V. Khomenko, E. Raymundo-Piñero, J.B. Parra, F. Béguin, The large electrochemical capacitance of microporous doped carbon obtained by using a zeolite template, *Adv. Funct. Mater.* 17 (2007) 1828–1836.
- [53] Y.S. Yun, S.Y. Cho, J. Shim, B.H. Kim, S.-J. Chang, S.J. Baek, et al., Microporous carbon nanoplates from regenerated silk proteins for supercapacitors, *Adv. Mater.* 25 (2013) 1993–1998.
- [54] A.B. Fuertes, M. Sevilla, High-surface area carbons from renewable sources with a bimodal micro-mesoporosity for high-performance ionic liquid-based supercapacitors, *Carbon* 94 (2015) 41–52.
- [55] W. Huang, H. Zhang, Y. Huang, W. Wang, S. Wei, Hierarchical porous carbon obtained from animal bone and evaluation in electric double-layer capacitors, *Carbon* 49 (2011) 838–843.